Chinese Chemical Letters 36 (2025) 109713

Contents lists available at ScienceDirect

Chinese Chemical Letters

journal homepage: www.elsevier.com/locate/cclet

Low-loading Pt anchored on molybdenum carbide-based polyhedral carbon skeleton for enhancing pH-universal hydrogen production

Zhuo Li[a,1], Peng Yu[b,1], Di Shen[a], Xinxin Zhang[a], Zhijian Liang[a], Baoluo Wang[a], Lei Wang[a,*]

[a] Key Laboratory of Functional Inorganic Material Chemistry, Ministry of Education of the People's Republic of China, Heilongjiang University, Harbin 150080, China

[b] Key Laboratory for Photonic and Electronic Bandgap Materials, Ministry of Education, School of Physics and Electronic Engineering, Harbin Normal University, Harbin 150025, China

ARTICLE INFO

Article history:
Received 4 February 2024
Revised 19 February 2024
Accepted 1 March 2024
Available online 11 March 2024

Keywords:
Organo-metallic phosphate framework
Low-Pt electrocatalyst
Wide-pH
Hydrogen evolution reaction
Water electrolysis

ABSTRACT

Developing high-efficient and low-loading Pt based catalyst is significant for the electrocatalytic pH-universal hydrogen evolution reaction (HER). Herein, the molybdenum carbide nanoparticles supported on the polyhedral N-doped carbon nanotube skeleton (MoC/NCT) composite has been synthesized by a pyrolysis of polyacid organo-metallic phosphate framework precursor. Then, only 2.15 wt% Pt are loaded on the MoC/NCT to form Pt-MoC/NCT catalyst, which performs superior HER activity and stability in entire pH range. Specially, the overpotentials of 22 and 74 mV are respectively attained at 10 mA/cm^2 in 1.0 mol/L KOH and 0.5 mol/L H_2SO_4 electrolytes, approaching or even exceeding commercial Pt/C. More importantly, it can be used as excellent catalyst for efficient hydrogen production at 0–14 pH range. Density functional theory (DFT) calculations demonstrate that the interaction between MoC and Pt leads to the electron redistribution at the corresponding interfaces and the downward shift of the d-band centers, thus optimizing H* adsorption and desorption for promoting the HER activity. Besides, the unique three-dimensional network structure is conductive to the transmission of mass and electrons. In the application of both alkaline and acidic electrolysers, only 1.52 V voltage of solar panel can drive a hydrogen production current density of 10 mA/cm^2.

Hydrogen energy is a clean, green and storable energy carrier with a higher energy density of 140 MJ/kg, which is 3 times than that of oil and 4.5 times than that of coal [1–4]. Its development and utilization have the potential to substitute the usage of traditional fossil fuels [5–8]. In the context of carbon peaking and carbon neutralization, hydrogen energy is regarded as a disruptive technology direction for future energy transformation [9–11]. Water electrolysis is one of the most efficient ways to efficiently produce hydrogen using electricity generated from any renewable energy source, including solar, wind and water [12–15]. Platinum (Pt)-based noble metal materials always regarded as the most efficient cathodic hydrogen evolution reaction (HER) electrocatalysts of water electrolysis due to their low overpotentials and fast reaction kinetics [16–18]. However, the low crustal abundance (about 0.005 ppm in Earth's crust) and high cost limit their large-scale commercial application [19–22]. Hence, the design of Pt-based electrocatalysts with reduced Pt content, while simultaneously improving the Pt utilization rate and the electrocatalytic activity for HER, poses a significant research challenge.

Molybdenum (Mo), belonging to the class of transition metals, exhibits a diverse range of properties due to its rich d-electro structure and adjustable d-band center [23–25]. This enables it to readily form compounds with a variety of non-metallic elements, such as MoN, MoP and MoS_2 [26–29]. Transition metal interstitial compound molybdenum carbide (Mo_xC) possess high conductivity and structural controllability, exhibiting Pt-like hydrogen adsorption free energy and electrocatalytic activity [30,31]. Properly adjusting the crystal structure of Mo_xC can optimize the adsorption/desorption energy of intermediates, thus promoting the electrochemical HER kinetics [32]. Previous studies have shown that the electrocatalytic activity of molybdenum carbides towards HER follows the order of α-MoC_{1-x} < η-MoC < γ-MoC < β-Mo_2C [33]. Although Mo_2C exhibits the best electrocatalytic activity, its high affinity for hydrogen adsorption inhibits the desorption process, resulting in a decreased hydrogen production rate [34,35]. On the other hand, MoC forms weaker Mo–H bonds after hydrogen adsorption, making the hydrogen desorption easier, but the hydrogen adsorption strength is relatively weak [36]. Alternatively, introduc-

* Corresponding author.
E-mail address: wanglei0525@hlju.edu.cn (L. Wang).
[1] These authors contributed equally to this work.

https://doi.org/10.1016/j.cclet.2024.109713
1001-8417/

ing Pt with stronger hydrogen adsorption capability is beneficial to enhance HER activity [37]. Chen *et al.* constructed Pt-N-MoC catalysts through Pt-N dual doping strategy, effectively modulating the near Fermi level (EF) surface states of MoC, optimizing the adsorption and desorption of H*, and accelerating the kinetics of HER. Thus, the alkaline HER overpotential of the Pt-N-MoC catalyst was 39 mV at 10 mA/cm^2, outperforming N-MoC (216 mV) and MoC (243 mV) [38]. The above-mentioned studies suggest that the effective combination of Pt with carbide support can modify the surface electronic states of the catalyst or alter the structural properties of the carbon support at the atomic scale, thereby simultaneously reducing the amount of platinum used while enhancing its catalytic activity. Nevertheless, the interaction between MoC and Pt needs to be further explored, and the development of a pH-universal HER catalyst is more meaningful for sustainable energy sources.

Based on the above consideration, we have successfully fabricated the MoC nanoparticles (NPs) supported on the polyhedral N-doped carbon nanotube skeleton (MoC/NCT) composite through a pyrolytic polyacid organo-metallic phosphate framework precursor strategy. It can be used as a carrier to prepare Pt-MoC/NCT catalyst with a low-loading of 2.15 wt% Pt NPs. The unique three-dimensional network structure is favorable for mass and electrons transfer, as well as the optimized H* adsorption and desorption energy. As a result, Pt-MoC/NCT catalyst achieves small overpotentials of 22 and 74 mV at 10 mA/cm^2, and low Tafel slope of 36 and 66 mV/dec in 1.0 mol/L KOH and 0.5 mol/L H_2SO_4 electrolyte, respectively, which could be comparable to commercial Pt/C. Moreover, it also shows excellent HER activity at 0–14 pH-entire range electrolytes. Significantly, the electrolyser assembled with Pt-MoC/NCT as cathode has superior performance under both acidic and alkaline conditions. Our work provides an effective strategy for constructing low-Pt loading, high-efficient and pH-universal HER catalyst to accelerate the practical application of electrochemical hydrogen production.

The detailed synthetic process of Pt-MoC/NCT is illustrated in Fig. 1a. Firstly, the POM_{12}@ZIF8 was synthesized by 2-methylimidazole coordinating with Zn^{2+} ions and phosphomolybdic acid (POM_{12}). Then, the Co^{2+} was further introduced to form POM_{12}@ZIF8@ZIF67 precursor. Subsequently, the MoC/NCT composite was prepared after a pyrolysis in N_2 ambient. Finally, the Pt-MoC/NCT was synthesized by a traditional sodium borohydride reduction strategy. Also, the MoC/NC synthesized without using Co^{2+} was also prepared as carrier for loading Pt NPs by the same procedure. As the scanning electron microscopy (SEM) images shown in Figs. 1b and c, Pt-MoC/NCT exhibits polyhedral structures with the average size of 370 nm. Furthermore, the carbon nanotube structures (CNTs) grow on the polyhedral can be observed. In contrast, no CNTs structures can be found for Pt-MoC/NC synthesized without using Co^{2+} (Fig. S1 in Supporting information). It is indicated that the cobalt species can catalyze carbon source to form CNTs structures, which is consistence with previous studies [39]. The transmission electron microscopy (TEM) image further reveals hollow CNTs grow on polyhedral structure for Pt-MoC/NCT (Fig. 1d). The corresponding high-resolution TEM (HRTEM) image in Fig. 1e shows distinct lattice fringes with interplanar spacings of 0.229 and 0.226 nm corresponding to the (103) face of MoC and the (111) face of metallic Pt, respectively. It implies that the Pt nanoparticles (NPs) are well intimate contact with MoC NPs, which are embedded in the carbon substrate. Moreover, the Pt, Mo, C, N and O elements are homogeneous distributed as evidenced by elemental mapping images in Figs. 1f-l. The overlay image further confirms that the Pt NPs is uniformly dispersed on the surface of catalyst, especially concentrating on the surface of MoC NPs. The contents of Mo and Pt in Pt-MoC/NCT are respectively 18.95 and 2.15 wt% tested by inductively coupled plasma optical emission spectrometry (ICP-OES).

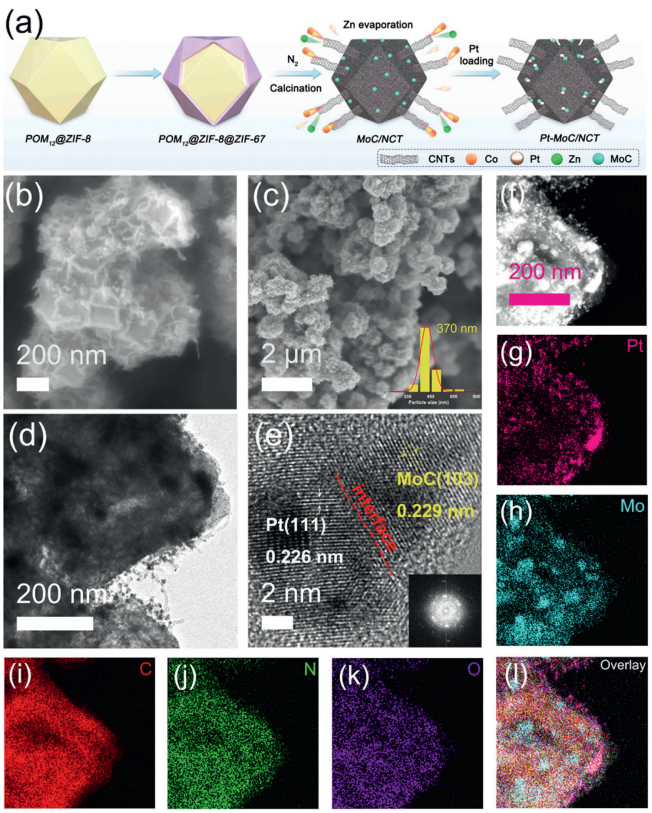

Fig. 1. (a) Illustrated scheme for the synthesis of Pt-MoC/NCT. (b, c) SEM (inset represents the particle size distribution), (d) TEM, (e) HRTEM, (f) HAADF-STEM images and (g-l) the corresponding elemental mapping images for Pt, Mo, C, N, O and overlay of Pt-MoC/NCT.

The crystalline phase structure was verified by X-ray powder diffraction (XRD) pattern. As displayed in Fig. 2a, the diffraction peaks 2θ located at 35.0°, 36.8°, 39.3°, 42.6°, 61.5°, 67.9° and 73.9° of MoC/NCT are ascribed to (101), (006), (103), (104), (110), (108) and (116) facet of MoC (PDF #08–0384), respectively. After loading Pt, the main diffraction peaks 2θ located at 39.8° corresponds to the (111) face of Pt (PDF #04-0802), which is closed to the (103) facet of MoC. Moreover, the broad diffraction peak at around 20°−30° indicates the presence of amorphous carbon. N_2 adsorption-desorption measurements were carried out to further characterize the material (Fig. 2b). All the samples exhibit type IV adsorption isotherms, indicating that the porous structures are mainly mesopores, which are concentrated at 2 nm. The specific surface area of MoC/NCT is 305.8 m^2/g. Furthermore, Pt-MoC/NCT represents similar pore size and specific surface area (349.8 m^2/g) to that of MoC/NCT, indicating that the introduction of Pt NPs could not destroy the pore structure. The unique three-dimensional porous structure and large specific surface area facilitate to expose a plenty of active sites, directly promoting the charge transfer along the one-dimensional CNTs structure. Besides, it is beneficial to maintain the structural integrity of catalyst and improve the stability during electrochemical process.

The composition and surface chemical structure were further investigated using X-ray photoelectron spectroscopy (XPS). The wide XPS spectrum reveals the presence of Pt, Mo, C, N and O in Pt-MoC/NCT (Fig. 2c). The high-resolution Mo 3d spectra of Pt-MoC/NCT and MoC/NCT can be decomposed into six peaks (Fig. 2d). Specially, the peaks located at 227.9 and 231.1 eV belong to the Mo–C bond, respectively. The other peaks located at 228.6/232.1 and 231.7/234.9 eV corresponds to Mo^{4+} and Mo^{6+}, which are originated from the surface oxidation products, such as MoO_2 and

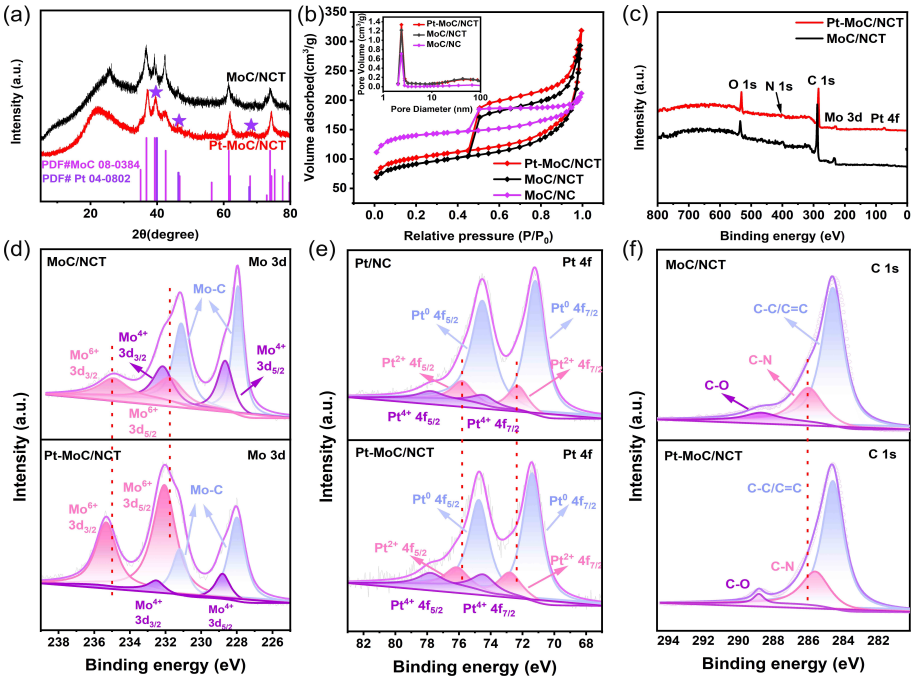

Fig. 2. (a) XRD patterns of Pt-MoC/NCT and MoC/NCT. (b) N_2 adsorption–desorption isotherms of Pt-MoC/NCT, MoC/NCT and MoC/NC. XPS spectra: (c) Wide and (d) Mo 3d spectra of Pt-MoC/NCT and MoC/NCT; (e) Pt 4f spectra of Pt-MoC/NCT and Pt/NC; (f) C 1s spectra of Pt-MoC/NCT and MoC/NCT.

MoO_3, since the surface of MoC is easily oxidized by air [40,41]. The Mo^{6+} peak of Pt-MoC/NCT positively shifts by 0.4 eV compared to that of the MoC/NCT, so the Mo loses electrons after loading Pt. Fig. 2e shows the high-resolution Pt 4f spectrum of Pt-MoC/NCT. The peaks at 71.2 and 74.5 eV are attributed to Pt^0 $4f_{7/2}$ and Pt^0 $4f_{5/2}$ of metallic Pt, respectively, while the peaks located at 72.3 and 75.8 eV are the Pt $4f_{7/2}$ and Pt $4f_{5/2}$ of Pt^{2+}. Additionally, the peaks located at 74.4 and 77.8 eV are the Pt $4f_{7/2}$ and Pt $4f_{5/2}$ of Pt^{4+}, attributing to the PtO and PtO_2, respectively. The Pt in Pt-MoC/NCT is obviously shifted to higher binding energy compared with Pt@NC. As illustrated in Fig. 2f, the high-resolution C 1s spectra of Pt-MoC/NCT and MoC/NCT can be decomposed into three peaks, including C–C/C=C (284.6 eV), C–N (286 eV) and C–O (288.6 eV). Compared to MoC/NCT, the C 1s peak of Pt-MoC/NCT negatively shifts 0.4 eV, indicating that the C in Pt-MoC/NCT gain electron from the Mo and Pt. The above results certify that the electron transfer occurs between Pt and MoC, which modulates the interfacial electronic structure to adjust the electrocatalytic performance. The high-resolution N 1s spectrum of Pt-MoC/NCT shows three peaks at 398.1, 399.1, and 400.7 eV (Fig. S3 in Supporting information), which corresponds to the pyridine nitrogen, pyrrolic nitrogen, and graphitic nitrogen, respectively.

The X-ray absorption near-edge structure (XANES) spectra are given in Fig. 3a. Generally, the white line (WL) intensity of the Pt L_3-edge of corresponds to the electron transfer from the Pt $2p_{3/2}$ core to the 5d orbitals, which can reveal the density of unoccupied states associated with the Pt 5d orbitals. The WL intensity of Pt-MoC/NCT is slightly higher than that of Pt foil, indicating that fewer electrons exist in the 5d orbital due to the electrons transfer from the Pt *via* either the Pt–O/C bond or Pt–Mo bond, consistent with the above XPS result. Moreover, the Fourier transform extended X-ray absorption fine structure (FT-EXAFS) spectra of Pt L_3-edge reveal the presence of Pt–O/C, Pt–Pt and Pt–Mo bonds in Pt-MoC/NCT (Fig. 3b). The corresponding fitting curves are shown in Figs. S4a and b (Supporting information), and the fitting results include bond distance (R) and coordination number (n) are provided in Table S1 (Supporting information). For Pt-MoC/NCT, the first shell peak is the Pt–O/C bond (R: 2.14 Å, n: 2.37), and the second shell peak is the Pt–Pt bond (R: 2.97 Å, n: 12.62) and Pt–Mo bond (R: 2.74 Å, n: 3.14). Due to the close position of the Pt–Pt and Pt–Mo bonds in Pt-MoC/NCT, the wavelet transform (WT, $\kappa = 10$, $\sigma = 1$) contour plots of the Pt L_3-edge were used to further distinguish them. As illustrated in Fig. 3c, the Pt/NC demonstrates the Pt–O/C bond at *k*-space $k = 4.6$ $Å^{-1}$, Pt-MoC/NCT also shows the Pt–Mo resolved spectra at *k*-space $k = 6.0$ $Å^{-1}$ and Pt–Pt at *k*-space $k = 7.8$ $Å^{-1}$, with the Pt–Mo region being lower than the Pt–Pt region due to the lighter atomic mass of Mo. Moreover, the bond length and coordination number of the Pt–O/C and Pt–Pt bonds for Pt-MoC/NCT are increased compared to Pt/NC. The Mo K-edge XANES spectrum in Fig. 3d exhibits similar curve for Pt-MoC/NCT and MoC/NCT. However, the pre-edge peak energy of Pt-MoC/NCT is higher than that of MoC/NCT, indicating that the electron density around Mo is decreased by introducing Pt. The FT-EXAES spectrum in Fig. 3e reveals that the bond length of the Mo–Mo bond in Pt-MoC/NCT is 2.97 Å, slightly longer than that in MoC/NCT. The maximum intensity of the WT-EXAFS for Pt-MoC/NCT (7 $Å^{-1}$) differs minimally from that of MoC/NCT (7.1 $Å^{-1}$) with a difference of approximately 0.1 $Å^{-1}$. It may be attributed to the introduction of Pt causing some partial strain effects as shown in Fig. 3f. Therefore, it can further determine that the Pt NPs have been successfully anchored to the MoC/NCT surface through Pt–O/C and Pt–Mo bonds.

The electrochemical performance was first estimated in 1 mol/L KOH electyrolyte, and the polarization curves were obtained by linear sweep voltammetry (LSV) as shown in Fig. 4a. The Pt-MoC/NCT displays the best HER activity with an onset potential (E_{onset}) almost zero, which is similar to that of 20% Pt/C. Moreover, the current densities of 10 and 100 mA/cm^2 can be obtained for Pt-MoC/NCT with only 22 and 85 mV overpotentials (Fig. 4b), which are much lower than those of MoC/NCT (169 and 278 mV), MoC/NC (190 and 311 mV), Pt-MoC/NC (33 and 243 mV) and Pt/C (28 and 94 mV). It is further demonstrated that the introduction of low-content Pt could decrease the overpotentials, while the Pt-MoC/NCT respectively shows decreased 147 and 193 mV overpo-

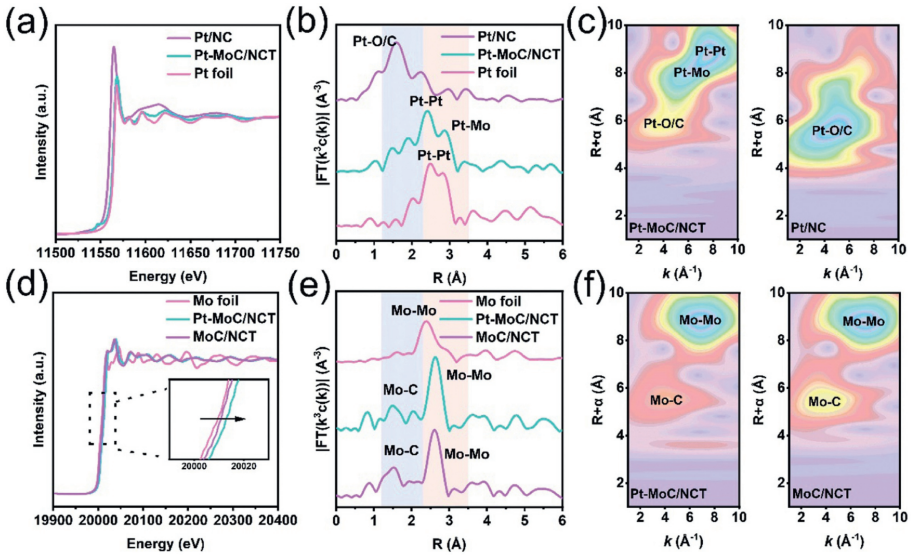

Fig. 3. (a) Normalized XANES spectra. (b) FT-EXAFS spectra and (c) wavelet-transform contour plots of Pt-MoC/NCT and Pt/NC at Pt L_3-edge. (d) Normalized XANES spectra, (e) FT-EXAFS spectra and (f) WT contour plots of Pt-MoC/NCT and MoC/NCT at Mo K-edge.

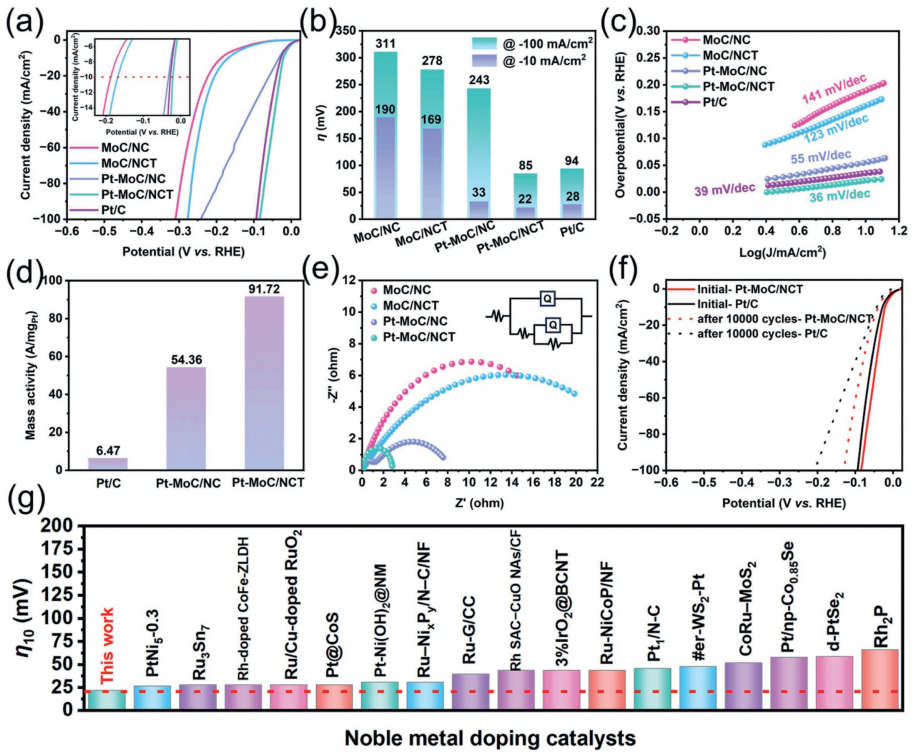

Fig. 4. HER performance in 1.0 mol/L KOH electrolyte. (a) LSV curves, (b) overpotentials at 10 and 100 mA/cm^2, (c) Tafel slopes, (d) mass activity at an overpotential of 20 mV (*vs.* RHE) and (e) corresponding nyquist plots of different catalysts. (f) Polarization curves for Pt-MoC/NCT and Pt/C before and after 10,000 cycles test. (g) Comparison the overpotentials of Pt-MoC/NCT with reported catalysts at 10 mA/cm^2.

tentials at 10 and 100 mA/cm^2. It is attributed to the MoC possesses the similar d-electronic structure to that of precious metal Pt, so the Pt-like property makes it can regulate the local electron density of Pt for exposing more active sites and enhancing electrocatalytic activity. Significantly, the lower overpotential of MoC/NCT before and after Pt loading compared with the corresponding MoC/NC. It is attributed to the introducting of Co species could facilitate to the formation of hollw CNT structures during the pyrolytic process, thus accelerating the electron transfer, ion transport and gas diffusion and improving electrocatalytic performance. Tafel slope is an important parameter to study the kinetics of electrocatalytic reaction. As displayed in Fig. 4c, the Tafel slope of the Pt-MoC/NCT sample was 36 mV/dec, which is much smaller than that of Pt-MoC/NC of 55 mV/dec, MoC/NCT of 123 mV/dec, MoC/NC of 141 mV dec^{-1} and Pt/C of 39 mV/dec. It is indicated that Pt-MoC/NCT performs the same H_2 evolution pathway as Pt/C (Volmer-Tafel pathway: $H^+ + e^- + * \rightarrow H^*$, $H^* + H^* \rightarrow H_2$) [42,43]. The smallest Tafel slope clearly reveals the abundant Pt active sites of Pt-MoC/NCT contributes to the ultrafast reaction kinetics.

The electrochemical specific surface area (ECSA) is proportional to the double-layer capacitance (C_{dl}) was measured by cyclic voltammetry (CV) in the voltage range of 0.4–0.60 V (*vs.* RHE), which could reflect the electrocatalytic activity. As shown in Fig. S5 (Supporting information), the C_{dl} value of Pt-MoC/NCT is 90.5 mF/cm^2, which is much higher than that of Pt-MoC/NC (87 mF/cm^2), MoC/NCT (43.5 mF/cm^2), MoC/NC (77.5 mF/cm^2) and Pt/C (72 mF/cm^2). Furthermore, the ECSA value of Pt-MoC/NCT calculated by C_{dl} is 2262.5 cm^2, which is higher than the other comparison samples (Fig. S6 in Supporting information), indicating the high HER activity of Pt-MoC/NCT. At an overpotential of 20 mV, the mass activity of Pt-MoC/NCT is 91.72 A/mg$_{Pt}$, about 14 times as that of Pt/C, greatly improving the utilization rate of Pt and has great practical application value (Fig. 4d). Turnover frequency (TOF) is the number of hydrogen molecules produced per second at each active site during HER process, which can reflect the intrinsic catalytic efficiency and catalytic capacity of each active site in the catalyst. As illustrated in Fig. S7e (Supporting information), the Pt-MoC/NCT shows the largest TOF value of 3.828 s^{-1} at a potential of −0.02 V in 1 mol/L KOH electrolyte compared to the Pt-MoC/NC (0.876 s^{-1}), MoC/NCT (0.136 s^{-1}) and MoC/NC (0.006 s^{-1}). It can be implied that Pt-MoC/NCT has the highest intrinsic electrocatalytic activity. In addition, the electrochemical impedance spectra (EIS) in Fig. 4e exhibits the fast HER kinetics of Pt-MoC/NCT at the interface between the catalyst and electrolyte. The lower charge transfer resistance of Pt-MoC/NCT is ascribed to the strong synergistic effect between MoC and Pt can significantly promote the electron transfer rate. Moreover, the overpotential of Pt-MoC/NCT shows only 20 mV positively shifts after 10,000 consecutive CV cycles at a current density of 10 mA/cm^2 (Fig. 4f). More importantly, it can stably operate for 18 h with tolerable change at a large current density of 210 mA/cm^2, demonstrating the potential application for large current water splitting (Fig. S8a in Supporting information). More importantly, the HER activity of Pt-MoC/NCT exceeds most of the reported noble metal-based catalysts in alkaline electrolyte as displayed in Fig. 4g and Table S3 (Supporting information). Notably, no obvious structural change can be observed for Pt-MoC/NCT after 10,000 CV cycles test as evidenced by SEM, TEM, ICP, XRD and XPS characterizations (Figs. S9-S11 in Supporting information), further demonstrating the excellent structural stability.

Considering that the HER typically utilizes Pt-based catalysts in acidic environments, the Pt-MoC/NCT catalyst with a low Pt loading was also tested in 0.5 mol/L H_2SO_4 electrolyte. It is evident from the results that the Pt-MoC/NCT exhibits superior HER activity as confirmed by low E_{onset} and overpotentials (Fig. 5a). In Fig. 5b, it is demonstrated that current densities of 10 and 100 mA/cm^2 can be achieved for Pt-MoC/NCT with overpotentials of merely 74 and 286 mV, respectively. The corresponding values are considerably lower than those observed for MoC/NC, MoC/NCT, and Pt-MoC/NC, and are comparable to those of Pt/C. As shown in Fig. 5c, the Pt-MoC/NCT exhibits a smaller Tafel slope of 66 mV/dec compared to Pt-MoC/NC (80 mV/dec), MoC/NC (203 mV/dec), MoC/NCT (270 mV/dec), closer to that of Pt/C of 61 mV/dec, also indicating that the HER process undergoes the Volmer-Heyrovsky step with the rate-determining step of Heyrovsky step. CV curves were conducted in the voltage range of 0.8–0.90 V (*vs.* RHE) to calculating the ECSA by testing C_{dl}. Fig. S12 (Supporting information) illustrates that the C_{dl} value of Pt-MoC/NCT is 32 mF/cm^2, much higher than Pt-MoC/NCT of 15.5 mF/cm^2, MoC/NC of 6 mF/cm^2 and MoC/NCT of 9 mF/cm^2. Additionally, the ECSA value of Pt-MoC/NCT is calculated to be 800 cm^2 based on C_{dl}, which surpasses the ECSA of other comparison samples (Fig. S13 in Supporting information). As displayed in Fig. 5d, the mass activity of Pt-MoC/NCT is 9.86 A/mg$_{Pt}$ at an overpotential of 20 mV, which is 8 times higher as that of Pt/C. The TOF value of Pt-MoC/NCT is 0.442 s^{-1} at a potential of −0.02 V in acidic media, surpassing Pt-MoC/NC (0.135 s^{-1}), MoC/NCT (0.094 s^{-1}), and MoC/NC (0.090 s^{-1}) (Fig. S7f in Supporting information). It is further indicated that Pt-MoC/NCT presents high intrinsic catalytic activity in both alkline and acidic medias. The EIS in Fig. 5e demonstrates a lower charge transfer resistance for Pt-MoC/NCT, implying the fast electron transfer, which is beneficial to the HER activity. Moreover, the current-time (*I-t*) curve in Fig. 5f reveals that the current density remains almost unchanged after 100 h test, further confirming its exceptional long-term stability. As illustrate in Fig. S8b (Supporting information), it can stably operate for 23 h at a large current density of 120 mA/cm^2 in 0.5 mol/L H_2SO_4, further indicating the potential application for large current water splitting. The outstanding HER performance of Pt-MoC/NCT in acidic electrolyte is comparable to that of most reported advanced noble metal-based electrocatalysts (Fig. 5g and Table S4 in Supporting information). To explore the HER performance of Pt-MoC/NCT over a wide pH range, the LSV curves were tested in electrolytes ranging from pH 0 to pH 14 (Fig. S14 in Supporting information). Interestingly, at pH 0–6, the overpotential of Pt-MoC/NCT at a current density of 10 mA/cm^2 gradually increases as the pH increases. On the other hand, at pH 7–14, the overpotential decreases with the pH increase. It suggests that the Pt-MoC/NCT exhibits dynamic HER performance across a wide pH range, indicating the enhanced pH-universal hydrogen production performance.

Based on the excellent HER performance of Pt-MoC/NCT, it can be further used as cathode to construct overall water splitting, and the commercial RuO_2 was used as anode. In 1 mol/L KOH electrolyte, the Pt-MoC/NCT||RuO_2 electrolyser only needs a voltage of 1.52 V at a current density of 10 mA/cm^2, lower than that of the Pt/C||RuO_2 electrolyser (Fig. 6a). Moreover, the *I-t* curve implies that the current for Pt-MoC/NCT||RuO_2 electrolyser only shows a negligible decrease after 40 h continuous operation in alkline media (inset in Fig. 6a), indicating the outstanding stability for overall water splitting. In 0.5 mol/L H_2SO_4 electrolyte, both Pt-MoC/NCT||RuO_2 and Pt/C||RuO_2 electrolysers exhibits a voltage of 1.52 V at a current density of 10 mA/cm^2 (Fig. 6b), Notably, the *I-t* curve in the inset in Fig. 6b demonstrates that Pt-MoC/NCT||RuO_2 electrolyser can continuously operate for 130 h in acidic media, further certifying its superior long-term stability. To demonstrate practical application potential, a solar-assisted water splitting device was assembled by using commercial solar panels (Figs. 6c and d). At an operated potential of 1.52 V, the noticeable H_2 and O_2 bubbles produces on the anode and cathode surfaces, signifying the successful conversion of low-voltage electricity generated by solar energy into chemical energy. The present innovation holds great promise for practical applications in future.

Density functional theory (DFT) calculations could provide further insight into the enhanced mechanism of HER activity. The three theoretical models of Pt (111), MoC, and MoC-Pt were constructed based on the above characterization results, and the possible H* adsorption sites on different models were also constructed (Figs. 7a-d, Figs. S15-S17 in Supporting information). The charge density difference shown in Fig. 7e indicates the presence of electron accumulation and transfer at the interface, suggesting a strong electron interaction between Pt and MoC. The Gibbs free energy of H* adsorption (ΔG_{H^*}) is an important parameter for assessing HER activity. Generally, when the absolute value ofΔG_{H^*} ($|\Delta G_{H^*}|$) is closer to zero, the H* desorption and adsorption will be easier, so the Pt shows a closer optimal HER activity. The ΔG_{H^*} value of the Pt-2 site at the MoC-Pt interface is approximately –0.19 eV (Fig. 7f), which is closer to the ΔG_{H^*} value of the Pt site on Pt (111) ($\Delta G_{H^*} = -0.10$ eV). It is noteworthy that the Mo-2 site at the MoC-Pt interface exhibits a ΔG_{H^*} value of approximately −0.69 eV, which is better than the ΔG_{H^*} value of the Mo site on MoC model ($\Delta G_{H^*} = -0.96$ eV). Numerous studies have indicated that the des-

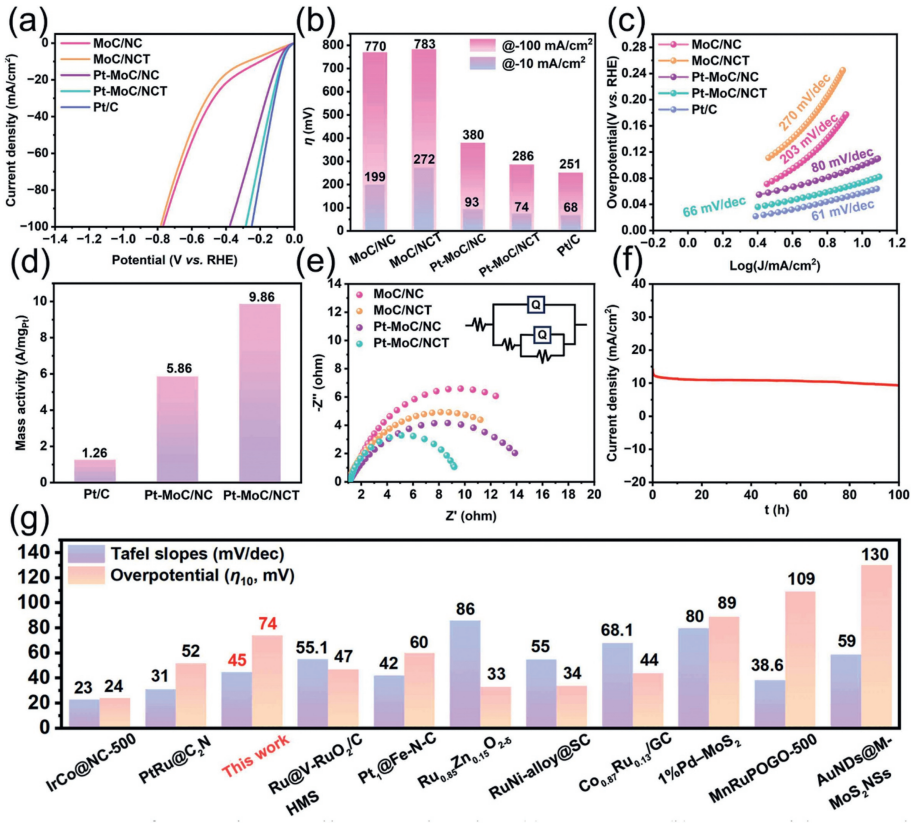

Fig. 5. HER performance in 0.5 mol/L H_2SO_4 electrolyte. (a) LSV curves, (b) overpotentials at 10 and 100 mA/cm^2, (c) Tafel slopes, (d) mass activity at an overpotential of 20 mV (*vs.* RHE) and (e) corresponding Nyquist plots of different catalysts. (f) *I-t* curve of Pt-MoC/NCT for 100 h test. (g) Comparison the overpotentials at 10 mA/cm^2 and Tafel slopes of Pt-MoC/NCT with the reported precious metal-based electrocatalysts.

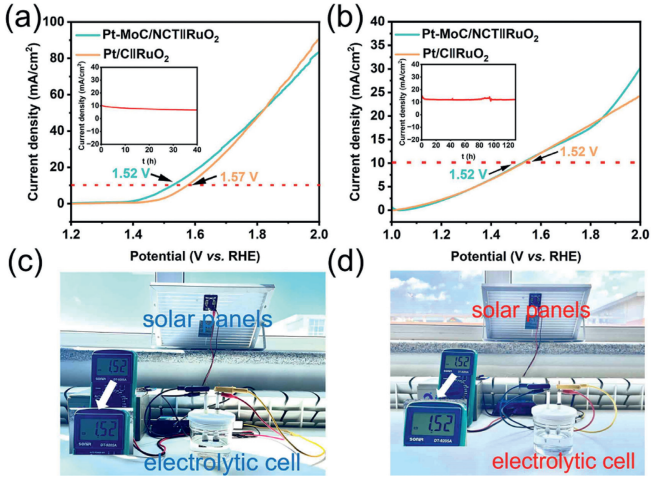

Fig. 6. Polarization curves for Pt-MoC/CNT||RuO_2 and Pt/C||RuO_2 electrolytic cells in (a) 1 mol/L KOH and (b) 0.5 mol/L H_2SO_4 electrolytes for Pt-MoC/NCT||RuO_2 and Pt/C||RuO_2. Insets are the corresponding *I-t* curves of Pt-MoC/CNT||RuO_2 electrolytic cells. Digital photographs of solar panel assisted water splitting device, for Pt-MoC/NCT||RuO_2 electrolytic cells in (c) 1 mol/L KOH and (d) 0.5 mol/L H_2SO_4 electrolytes.

orption of adsorbed H* is difficult when ΔG_{H^*} is less than 0 eV. The results demonstrate that the heterogeneous interfacial interaction of MoC-Pt can optimize the H* adsorption for enhancing HER activity compared with MoC model.

As depicted in Fig. 7g, the continuous distribution of the density of states (DOS) near the Fermi energy level indicates that the MoC-Pt model are metallic state, benefiting to improve electronic conductivity. To gain insights into the impact of d-electron modulation on the HER activity, calculations were performed to determine the partial DOS (PDOS) of Pt (111), MoC and MoC-Pt models. The DFT calculations reveal that the d-band center (ε_d) of MoC-Pt model shifts downwards to −1.20 eV, lower than that of MoC model (−0.78 eV), approaching to the Pt model (−2.19 eV) (Fig. S18 in Supporting information). The downward shift of ε_d for MoC-Pt model indicates the mutual modulation between Pt and MoC d-electrons. Such a decrease in ε_d leads to weaker and easier desorption of adsorped H* on the surface, thereby optimizing the ΔG_{H^*} and promoting the intrinsic electrocatalytic activity. The PDOS in Fig. 7h demonstrates that the energy levels of the Pt 5d and Mo 3d orbitals on the MoC-Pt model exhibit a substantial overlap below the Fermi energy level (in the darker region) in contrast to Pt (111) and MoC. In the MoC-Pt model, the certain Pt 5d orbitals are shifted to lower energy levels, indicating the strong bonding interactions between Pt and MoC. The work function (WF) can reflect the reaction rate of the HER, which could be calculated based on the scanning Kelvin probe (SKP) test (Fig. S19 in Supporting information). The WF values for Pt-MoC/NCT and Pt/C were determined to be 5.683 and 5.526 eV, respectively. The higher WF value of Pt-MoC/NCT suggests the stronger electron-donating ability, facilitating the reduction of H* to H_2 on Pt-MoC/NCT and thus enhancing the HER activity. Based on a series of performance tests and DFT calculations, the formation of MoC and Pt heterojunction facilitates electron transfer between the Mo and Pt, leading to the electron redistribution at the heterogeneous interfaces. It results in a downward shift of the d-band centers, optimizing the difficulty of H* desorption. Besides, the unique three-dimensional porous structures enable the exposure of plentiful active sites for promoting HER activity.

We have successfully designed the Pt-MoC/NCT catalyst with a low-Pt content of 2.15 wt% *via* a pyrolytic polyacid organo-metallic

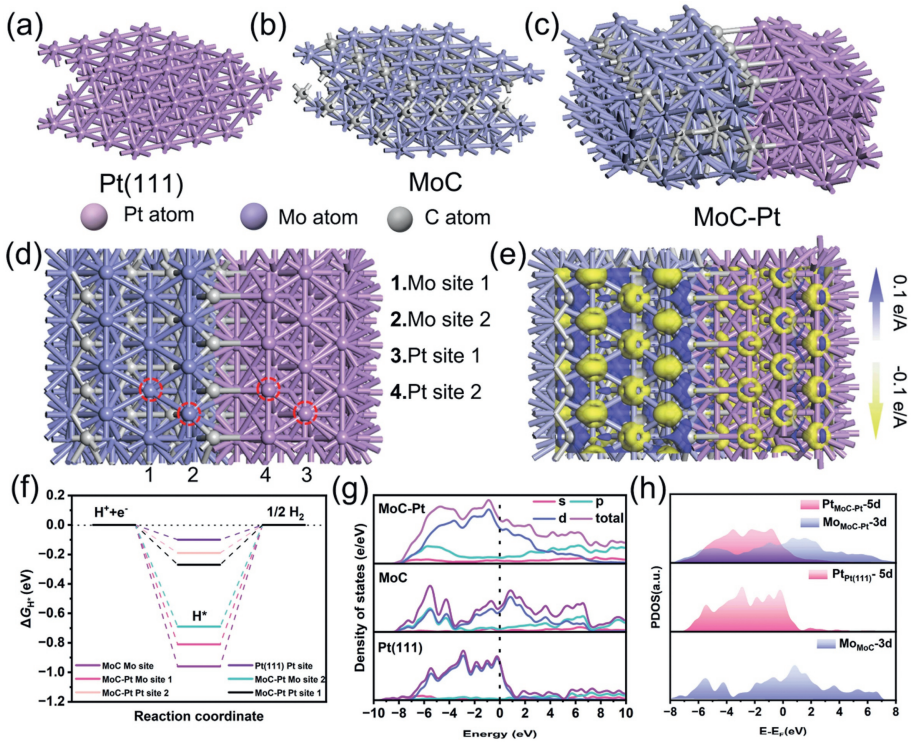

Fig. 7. (a) Pt (111), (b) MoC and (c) MoC-Pt models. (d) The different Mo and Pt sites for H* adsorption on MoC-Pt model. (e) The charge density difference of MoC-Pt model. (f) Free-energy diagram of ΔG_{H^*}. (g) DOS plots of Pt (111), MoC and MoC-Pt models. (h) PDOS of Pt 5d orbitals and Mo 3d orbitals in the MoC-Pt, Pt (111) and MoC.

phosphate framework precursor route. Due to the electron redistribution at the interfaces of MoC and Pt and the subsequent downward shift of the d-band centers, the Pt-MoC/NCT catalyst demonstrates excellent activity and stability for HER in 1.0 mol/L KOH and 0.5 mol/L H_2SO_4 electrolytes. It outperforms other state-of-the-art precious-based electrocatalysts and exhibits pH-universal performance for hydrogen production in the pH range of 0 to 14. The assembled electrolyzers require only 1.52 V voltage to achieve a current density of 10 mA/cm^2, which can be effectively driven by solar panels. This study presents a simple and effective strategy for the preparation of highly-efficient Pt catalysts with low-Pt content, making them promising candidates for HER electrocatalysts in various pH conditions.

Declaration of competing interest

The authors declare no conflict of competing interest.

Acknowledgments

We gratefully acknowledge the support of this research by the National Natural Science Foundation of China (No. 22179034), the Natural Science Foundation of Heilongjiang Province (No. ZD2023B002).

Supplementary materials

Supplementary material associated with this article can be found, in the online version, at doi:10.1016/j.cclet.2024.109713.

References

[1] Y. Gu, A.P. Wu, Y.Q. Jiao, et al., Angew. Chem. Int. Ed. 60 (2021) 6673–6681.
[2] T.T. Chao, W.B. Xie, Y.M. Hu, et al., Energy Environ. Sci. 17 (2024) 1397–1406.
[3] Y. Cheng, H.Y. Chen, L.F. Zhang, et al., Adv. Mater. 36 (2024) 202313156.
[4] Y.Q. He, F. Yan, X. Zhang, et al., Adv. Energy Mater. 13 (2023) 2204177.
[5] Y.H. Li, C.K. Peng, H.M. Hu, et al., Nat. Commun. 13 (2022) 2204177.
[6] M.H. Ning, F.H. Zhang, L.B. Wu, et al., Energy Environ. Sci. 15 (2022) 3945–3957.
[7] N.K. Oh, J. Seo, S. Lee, et al., Nat. Commun. 12 (2021) 4606.
[8] Z.H. Wang, D.L. Liu, Y. Zhang, et al., Appl. Phys. Lett. 123 (2023) 083901.
[9] M.Q. Liu, J.A. Wang, W. Klysubun, et al., Nat. Commun. 12 (2021) 5260.
[10] L.G. Li, S.H. Liu, C.H. Zhan, et al., Energy Environ. Sci. 16 (2023) 157–166.
[11] T. Liu, P. Li, N. Yao, et al., Angew. Chem. Int. Ed. 58 (2019) 4679–4684.
[12] M.Y. Wu, X.L. Fan, W.B. Zhang, et al., Chin. Chem. Lett. 35 (2024) 109258.
[13] Y.P. Zhu, K. Fan, C.S. Hsu, et al., Adv. Mater. 35 (2023) 2301133.
[14] L.M. Wang, L.L. Zhang, W. Ma, et al., Adv. Funct. Mater. 32 (2022) 2203342.
[15] Q. Zhou, Q.H. Bian, L.L. Liao, et al., Chin. Chem. Lett. 34 (2023) 107248.
[16] L.Y. Zeng, Z.L. Zhao, Q.Z. Huang, et al., J. Am. Chem. Soc. 145 (2023) 21432–21441.
[17] Z.P. Wang, Z.P. Lin, Y.L. Wang, et al., Adv. Mater. 35 (2023) 2302007.
[18] Y.P. Li, W.T. Wang, M.Y. Cheng, et al., Adv. Mater. 35 (2023) 2206351.
[19] Y.Q. Sun, K. Xu, Z.H. Zhao, et al., Appl. Catal. B: Environ. 278 (2020) 119284.
[20] Q.S. Gao, W.B. Zhang, Z.P. Shi, L.C. Yang, Y. Tang, Adv. Mater. 31 (2019) 1802880.
[21] H.S. Hu, Z.R. Zhang, Y.W. Zhang, et al., Energy Environ. Sci. 16 (2023) 4584–4592.
[22] L.Q. Wang, Z.P. Xu, C.H. Kuo, J. Peng, et al., Angew. Chem. Int. Ed. 62 (2023) e202311937.
[23] J. Wang, T. Liao, Z.Z. Wei, et al., Small Methods 5 (2021) 2000988.
[24] T.F. Li, T.Y. Lu, X. Li, et al., ACS Nano 15 (2021) 20032–20041.
[25] Y.J. Zhang, R.H. Lu, C. Wang, Y. Zhao, L.M. Qi, Adv. Funct. Mater. 33 (2023) 2303073.
[26] X.N. Zang, W.S. Chen, X.L. Zou, et al., Adv. Mater. 30 (2018) 1805188.
[27] W.Q. Han, J. Ning, Y. Long, et al., Adv. Energy Mater. 13 (2023) 2300145.
[28] L.B. Wu, F.H. Zhang, S.W. Song, et al., Adv. Mater. 34 (2022) 2201774.
[29] H.M. Jiang, L.T. Yan, S. Zhang, et al., Nano-Micro Lett. 13 (2021) 215.
[30] Y.F. Ma, M. Chen, H.B. Geng, et al., Adv. Funct. Mater. 30 (2020) 2000561.
[31] J.B. Wu, J.W. Su, T. Wu, et al., Adv. Mater. 35 (2023) 2209954.
[32] M.H. Hu, B.C. Liu, H.Y. Chen, et al., Appl. Catal. B: Environ. 322 (2023) 122131.
[33] C. Wan, Y.N. Regmi, B.M. Leonard, Angew. Chem. Int. Ed. 53 (2014) 6407–6410.
[34] M. Zhou, X.L. Jiang, W.J. Kong, et al., Nano-Micro Lett. 15 (2023) 166.
[35] Y. Yang, Y.M. Qian, Z.P. Luo, et al., Nat. Commun. 13 (2022) 7225.
[36] C.F. Yang, R. Zhao, H. Xiang, et al., Nano Energy 98 (2022) 107232.
[37] W. Wang, Y.X. Wu, Y.X. Lin, et al., Adv. Funct. Mater. 32 (2022) 2108464.
[38] M. Chen, L.H. Hu, L. Xu, et al., Small Methods 7 (2023) 2300308.
[39] X. Liu, L. Wang, G.Y. Zhang, et al., Chem. Eng. J. 414 (2021) 127569.
[40] T. Ouyang, Y.Q. Ye, C.Y. Wu, K. Xiao, Z.Q. Liu, Angew. Chem. Int. 58 (2019) 4923–4928.
[41] X. Huang, J. Wang, H.B. Tao, et al., J. Catal. 389 (2020) 461–467.
[42] P. Liu, X. Zhang, J. Fei, et al., Adv. Mater. 36 (2024) e2310591.
[43] A. Mosallanezhad, C. Wei, P.A. Koudakan, et al., Appl. Catal. B: Environ. 315 (2022) 121534.